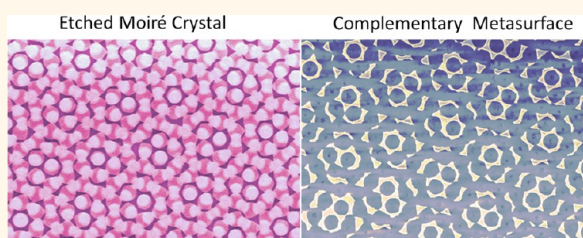


# Moiré Nanosphere Lithography

Kai Chen,<sup>\*,†,‡</sup> Bharath Bangalore Rajeeva,<sup>§</sup> Zilong Wu,<sup>§</sup> Michael Rukavina,<sup>§</sup> Thang Duy Dao,<sup>†,‡</sup> Satoshi Ishii,<sup>†,‡</sup> Masakazu Aono,<sup>†,‡</sup> Tadaaki Nagao,<sup>\*,†,‡</sup> and Yuebing Zheng<sup>\*,§</sup>

<sup>†</sup>National Institute for Materials Science, International Center for Material Nanoarchitectonics (MANA), Tsukuba, 305-0044, Japan, <sup>‡</sup>CREST, Japan Science and Technology Agency, 4-1-8 Honcho, Kawaguchi, Saitama, 332-0012, Japan, and <sup>§</sup>Department of Mechanical Engineering, Materials Science and Engineering Program, and Texas Materials Institute, The University of Texas at Austin, Austin, Texas 78712, United States

**ABSTRACT** We have developed moiré nanosphere lithography (M-NSL), which incorporates in-plane rotation between neighboring monolayers, to extend the patterning capability of conventional nanosphere lithography (NSL). NSL, which uses self-assembled layers of monodisperse micro/nanospheres as masks, is a low-cost, scalable nanofabrication technique and has been widely employed to fabricate various nanoparticle arrays. Combination with dry etching and/or angled deposition has greatly enriched the family of nanoparticles NSL can yield. In this work, we introduce a variant of this technique, which uses sequential stacking of polystyrene nanosphere monolayers to form a bilayer crystal instead of conventional spontaneous self-assembly. Sequential stacking leads to the formation of moiré patterns other than the usually observed thermodynamically stable configurations. Subsequent O<sub>2</sub> plasma etching results in a variety of complex nanostructures. Using the etched moiré patterns as masks, we have fabricated complementary gold nanostructures and studied their optical properties. We believe this facile technique provides a strategy to fabricate complex nanostructures or metasurfaces.



**KEYWORDS:** nanosphere lithography · moiré nanosphere lithography · sequential stacking · moiré pattern · plasmon · metasurface

Nanosphere lithography (NSL), also known as colloidal lithography, employs a monolayer or bilayer of close-packed colloidal spheres as masks to create patterns on the underneath substrates.<sup>1</sup> Compared with traditional lithographic tools such as photolithography, e-beam lithography (EBL), and focused-ion beam (FIB) milling, NSL holds great advantages because of its high throughput and low cost. In particular, NSL has been widely used to fabricate periodic plasmonic metal nanoparticle arrays, resulting in triangular-shaped and quasi-spherical nanoparticles from monolayer and bilayer sphere masks, respectively.<sup>2,3</sup> Other shapes of nanostructures, such as nanodisks,<sup>4,5</sup> nanocrescents,<sup>6–8</sup> and nanorings,<sup>9</sup> have also been fabricated through a multistep fabrication process involving dry etching and/or angled deposition.<sup>10–13</sup> These nanostructures with miscellaneous shapes are promising candidates for a number of applications, such as surface-enhanced spectroscopy,<sup>7,14</sup> photocatalysis,<sup>15</sup> active plasmonics,<sup>16–19</sup> and biochemical sensing.<sup>20,21</sup> Very recently, Nemiroski and colleagues have expanded the capability of NSL *via* sequential metal deposition from different angles through

plasma-etched microspheres to fabricate periodic complex metasurfaces.<sup>22</sup>

In general, the colloidal sphere masks are fabricated with various methods such as drop-casting, spin-coating, and convective self-assembly.<sup>23–26</sup> The quality of the masks is critical for achieving well-defined metal nanoparticle arrays. Tremendous efforts have been made to obtain high-quality monolayer or bilayer colloidal layers.<sup>26–28</sup> In particular, convective self-assembly has been developed for large-area patterning in horizontal<sup>25,29</sup> or vertical versions,<sup>24</sup> where colloidal spheres self-assemble into close-packed crystals as a result of the capillary force and hydrodynamic force. The crystals formed this way assume configurations with minimal free energy, leading to a hexagonal-close-packing (HCP) pattern for a monolayer crystal and face-centered-cubic (FCC) pattern for a multilayer crystal. In practice, the crystalline structure is complicated by substrate defects and external disturbances during the self-assembly process. Usually, HCP and FCC structures coexist for bilayer or bulky crystals together with structural defects such as cracks, vacancies, and dislocations. Choi *et al.* took advantage of the various crystalline

\* Address correspondence to  
Chen.Kai@nims.go.jp;  
Nagao.Tadaaki@nims.go.jp;  
zheng@austin.utexas.edu.

Received for review February 11, 2015  
and accepted May 28, 2015.

Published online May 28, 2015  
10.1021/acsnano.5b00978

© 2015 American Chemical Society

structures and demonstrated versatile nanopatterning based on reactive ion etching (RIE) of bilayer and trilayer crystals.<sup>30,31</sup> Still, the self-assembly process has limited the colloidal crystalline structures to a few configurations due to the energy minimization. As a result, it has remained challenging to further expand the morphologies of nanostructures that can be achieved with NSL.

Herein, we add another twist for nanopatterning with NSL. Unlike conventional formation of a bilayer crystal in a single spontaneous self-assembly step, we sequentially construct a bilayer crystal in a layer-by-layer fashion from monolayers of colloidal spheres at the water–air interface. This sequential packing allows for the formation of moiré patterns through the in-plane twist or rotation between the ordered domains in the bottom and top layers. O<sub>2</sub> plasma etching on the bilayer moiré crystals leads to a variety of unorthodox nanopatterns. Moiré patterns, the superposition of periodic layers, have been used for image processing,<sup>32</sup> anticounterfeit measures,<sup>33–35</sup> and refractive index sensing.<sup>36</sup> More recently, plasmonic quasicrystals have been fabricated using moiré patterns as masks.<sup>37,38</sup> These plasmonic quasicrystals could offer a broadband, polarization-independent response showing potential for novel light-trapping techniques.<sup>39–41</sup>

Moiré NSL (M-NSL) was coined for our proposed technique to emphasize the formation of moiré crystals with this simple yet highly effective extra step. We used these etched structures as masks to fabricate the complementary gold nanostructures with tunable optical properties. M-NSL has considerably expanded the capability of conventional NSL and provided a new strategy to engineer exotic plasmonic nanoantennas<sup>42,43</sup> and metasurfaces.<sup>44–46</sup>

## RESULTS AND DISCUSSIONS

**Colloidal Bilayer Formation.** Figure 1a illustrates the experimental setup we used for the formation of colloidal layers as masks for M-NSL. The polystyrene (PS) nanospheres self-assemble into a close-packed monolayer at the air/water interface (see Methods section). Subsequent water draining transfers the monolayer onto a clean substrate or onto another monolayer already deposited on the substrate (indicated as “substrate” in Figure 1a). The container of the water reservoir is inclined at  $\sim 5^\circ$  to the horizontal surface, which helps to drive the floating monolayer toward the lower side of the container where the substrate is located. As the water is slowly draining out of the container, the lower corner also forms a confined environment for the floating monolayer, facilitating the stacking of the second layer on the substrate.

Compared with conventional self-assembly process, this sequential deposition of one monolayer on top of another provides the opportunity for the in-plane rotation between the two layers. The relative rotation

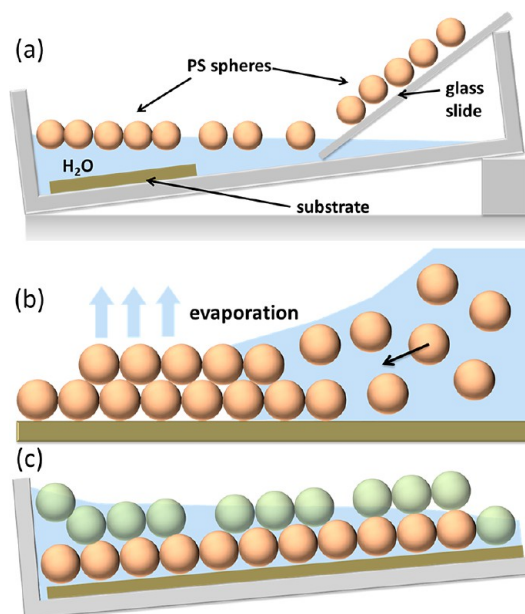


**Figure 1.** (a) Illustration of the setup for the formation of monolayer and bilayer PS spheres at the water–air interface. The sizes of the components are not scaled to their actual dimensions. The substrate is either a clean glass slide for the first monolayer deposition or an already-deposited monolayer ready for stacking of the second layer. (b) Cross-sectional illustration of conventional spontaneous self-assembly process for the formation of bilayer crystals. The spheres in the top layer reside in the interstices of the bottom layer dictated by thermodynamic stability. (c) Cross-sectional illustration of layer-by-layer sequential stacking for colloidal bilayer formation. The spheres in the top layer can reside on the top and on the shoulder of the spheres of the bottom layer as well as in the interstices of the neighboring spheres of the bottom layer. The different color for the spheres used in (c) is just for the sake of clarity between the first and second layer. The spheres are the same.

transforms the yielded structures of bilayer crystals and leads to the formation of moiré patterns. The bilayer formation process with spontaneous self-assembly and layer-by-layer stacking is schematically illustrated in Figure 1b and c, respectively.

In conventional spontaneous self-assembly as shown in Figure 1b, the attractive capillary force between the spheres enables the formation of close-packed bilayer crystals on substrates. Water flows to this region bringing more colloidal spheres and driving the continuous growth of the crystal. As the water evaporates from the colloidal crystals, the spheres in the top layer settle down on the interstices of the bottom layer because this configuration is thermodynamically favored. Experimentally, other configurations may coexist due to the defects and the small free-energy difference among the configurations. However, it has remained challenging to control the formation of different configurations, limiting their application as lithography masks. In our sequential stacking of bilayer crystals as illustrated in Figure 1c, an additional tuning factor is introduced: the relative in-plane rotation between the top and bottom layer. During the stacking process, the PS spheres in the top

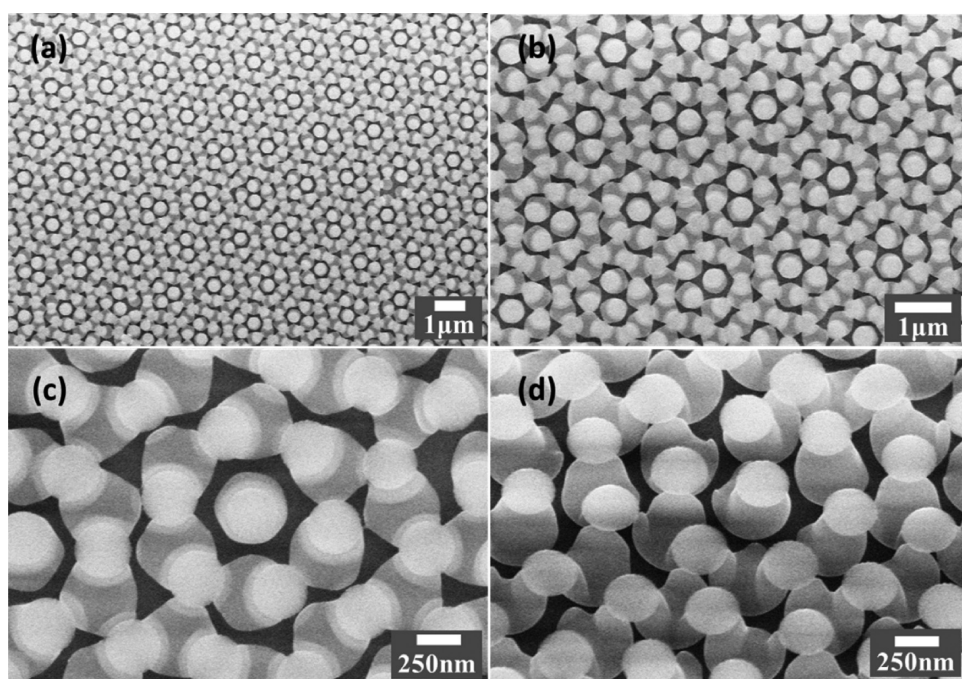


**Figure 2.** SEM images of one type of nanopattern of a bilayer crystal after RIE. Panels a, b, and c have different magnifications, and panel d shows a 30° tilted view of the same area as in panel c.

layer are joined together by the van der Waals force, and thus they lack freedom of movement, unlike those in the conventional method illustrated in Figure 1b. Furthermore, the top layer is confined by the water front and the container boundary. As a result, the positioning of the PS spheres in the top layer is considerably affected, and they not only can stay in the interstices of neighboring spheres in the bottom layer but also stay on top or shoulder of the spheres in the bottom layer, which are considered not stable and inaccessible in conventional spontaneous self-assembly. The van der Waals force is strong enough to ensure that the positioning of the top layer is not affected as the water dries off.

The positioning freedom of the top layer over the bottom layer opens up a new window of opportunities for tuning patterns. The rotational disorder of the top layer spheres results in the formation of moiré patterns as detailed later in the text. An equivalent scenario is observed in the case of graphene, wherein twisted adjacent layers are observed, in turn yielding the patterns.<sup>47</sup> In a separate work, secondary sputtering lithography and block copolymer moiré superstructures have been employed for creating various superlattice structures.<sup>48,49</sup> Hence, the usage of moiré patterns has proved to be a versatile technique for the formation of complex superlattices and plasmonic nanostructures.<sup>37,38,50,51</sup> With the ability to incorporate moiré patterns in NSL, we have managed to generate complex nanopatterns in a high-throughput and low-cost way.

**Complex Nanopatterning.** After construction of the bilayer crystals with sequential stacking, the samples

were exposed to O<sub>2</sub> RIE. Figure 2 shows the scanning electron microscopy (SEM) images of one type of nanopattern of the bilayer crystals after the O<sub>2</sub> etching. In all the panels, the top and bottom layers are distinguishable based on the contrast of the image. The top layer appears white, while the bottom layer appears grayish with the void space between the etched spheres as black.

Figure 2a and b show SEM images of one type of nanopattern with different magnification, and Figure 2c shows a zoom-in SEM image of a “repeating” unit of the pattern: a star-like void pattern (black region) surrounded by six similar features. It is clear that not all the spheres in the top layer dwell on the interstices of the spheres in the bottom layer. The colloidal spheres in the bottom layer no longer appear spherical after the dry etching due to the masking of the top layer, as evidenced in Figure 2c and d. It is also noted that, as shown in Figure 2a and b, the configuration of each unit is not exactly the same, and thus the structure does not precisely repeat itself. However, the units do have high resemblance to each other. The variation can be further minimized when the patterns are fabricated with defect-free high-quality monolayers of colloidal spheres.

Furthermore, other components with different shapes can be systematically added to the “repeating” unit to build more complex patterns, as shown in Figure 3. Similar to Figure 2, the white, gray, and black regions in the SEM images of Figure 3 correspond to the top layer, bottom layer, and the void spaces between the spheres. From panel a to d, the “repeating”

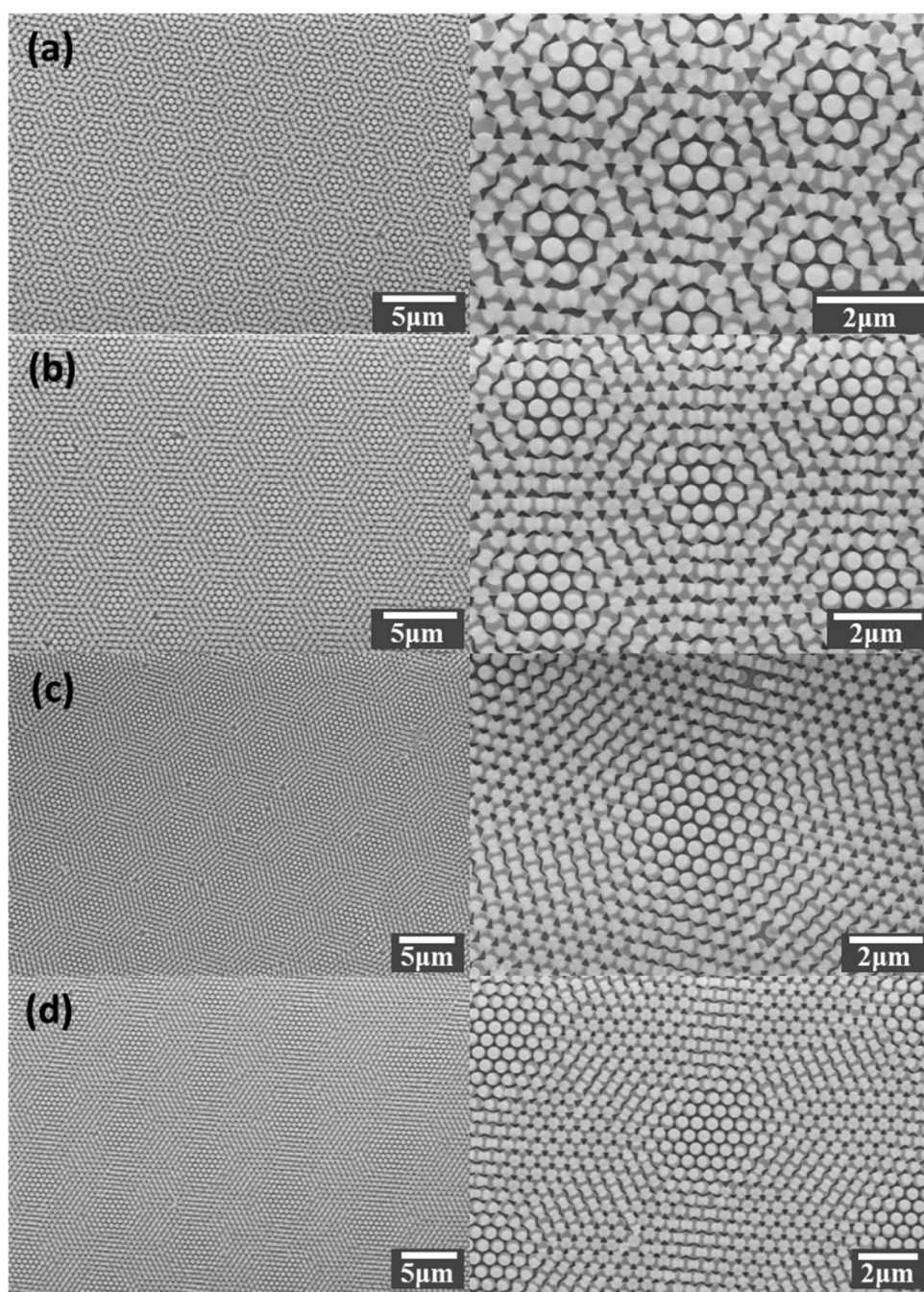


**Figure 3.** SEM images of a series of gradually changing patterns: the unit is growing bigger from top to bottom. The left column gives a broad overview for each pattern, and the right column gives a zoom-in view of each “repeating” unit.

unit grows in size while retaining the hexagonal spatial arrangement, which is also the geometrical configuration for colloidal monolayers. As the unit becomes bigger, its central region, where the top spheres reside almost exactly on the bottom spheres, also becomes bigger and its surrounding region is filled with more voids of different shapes such as triangle, curved shape, and other irregular shapes. All the patterns exhibit a long-range order with few scattered defects (Figure 3). Notably, the intricate patterns exhibit high symmetry. As shown in Figure 3d, the triangular voids

and the curved voids collocate with each other in a way that either group exhibits 6-fold rotational symmetry.

In addition to those large-scale regular complex patterns, smaller irregular patterns were also created during the M-NSL process. Figure 4 shows star-like patterns with the variable arrangements of a “repeating” unit. The individual star-like structure is similar to the one in the central part of the “repeating” unit in Figure 2c. However, the individual star-like structures can be arranged as triplets (Figure 4a), twins (Figure 4a and b), or well-separated individuals (Figure 4b).

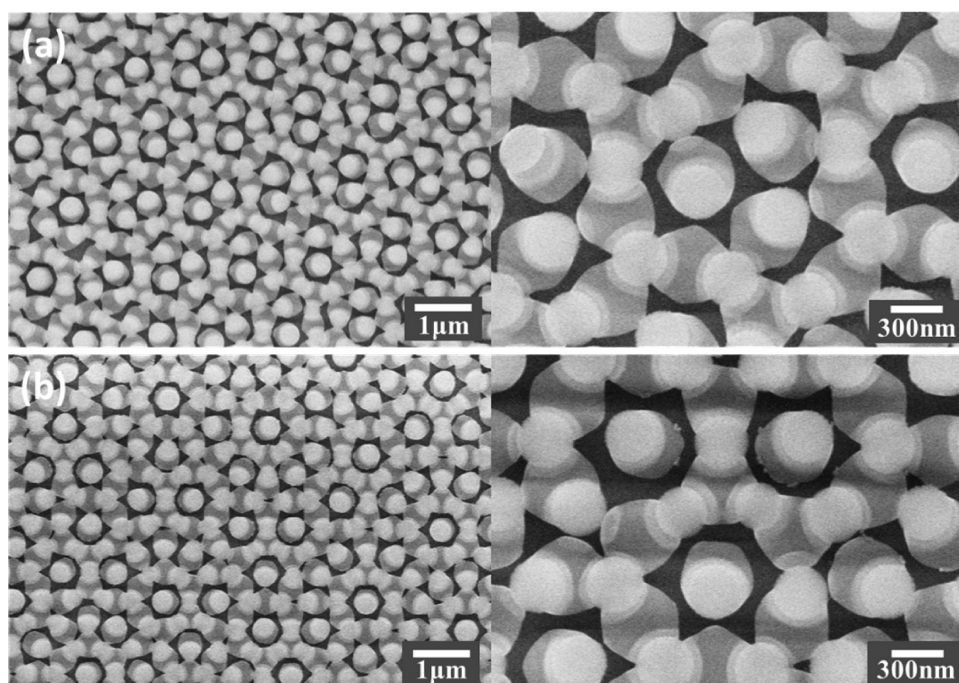


**Figure 4.** SEM images of star-like nanopatterns with variable arrangements: (a) star-like patterns arranged as triplets and (b) separated star-like patterns. Left and right columns are overview and zoom-in images, respectively.

Conventional spontaneous self-assembly cannot achieve those elaborate patterns as discussed above. When bilayer colloidal crystals fabricated from spontaneous self-assembly are exposed to  $O_2$  etching, the vast majority of the nanovoids are triangular-shaped interstices with few other patterns caused by defects in the crystals (Figure S1, Supporting Information). By contrast, M-NSL is capable of producing both triangular interstices and other variants, as shown in Figure 5.

**Mechanism of Pattern Formation.** The M-NSL considerably expands the variety of resulting nanopatterns in comparison to conventional NSL because the top layer has rotational and translational degrees of freedom. The origin of the structures shown in the above SEM images can be explained by considering the differences in the relative rotation angle between the top and bottom monolayers, *i.e.*, the moiré patterns.

In the case of conventional NSL, which results in triangular interstices (Figure S1, Supporting Information), the relative rotation between the top and bottom layers is regarded as zero and the translation of the top layer makes the spheres reside in the interstitial sites of the bottom layer due to thermodynamic stabilization. A perfect alignment of the two layers where all the spheres of the layers are on top of each other corresponds to zero rotation and translation. Figure 6 depicts the mechanism for the formation of various patterns based on the variable rotation angles.

The schematics in Figure 6a–d correspond to the patterns in the SEM images of Figure 3a–d. A decrease in the relative rotation angle between the top and bottom layers results in an increase of the unit size and

the periodicity of the moiré patterns. With a low rotation angle of below  $10^\circ$ , a few triangular interstices form (Figure 3c and d) because of the existence of areas with the top layer spheres in the interstices of the bottom layer similar to the conventional NSL. A larger rotation angle will result in the smaller unit in the moiré patterns and form more complex patterns (Figure 3a and b). Due to the numerous mismatch possibilities, a minute change in the relative angle can result in different patterns. Further increase of the rotation angle above  $30^\circ$  results in the repetition of patterns due to the hexagonal symmetry of the sphere layers. It should be noted that we use solid circles to represent the spheres in the top (gray) and bottom (black) layers in Figure 6. However, as shown in Figure 2, the spheres in the bottom layers are no longer spherically shaped after dry etching, which accounts for the discrepancy between the schematics and SEM images.

In our current experimental setup, the rotation angle between the top and bottom layer was not deliberately controlled, and all the demonstrated moiré patterns were fabricated on the same single substrate. However, it is possible to fabricate large-area patterns on substrates or a single moiré pattern on an individual substrate by creating monolayers of spheres with large single-crystalline domains and deliberately controlling the rotation angle between the top and bottom layers. It is noted that Figure 6 illustrates the ideal cases of the experiments: two single-crystal layers with the same period. In practice, the period can vary to some degree and become incommensurate. Thus, it is possible to form photonic quasicrystals using our proposed

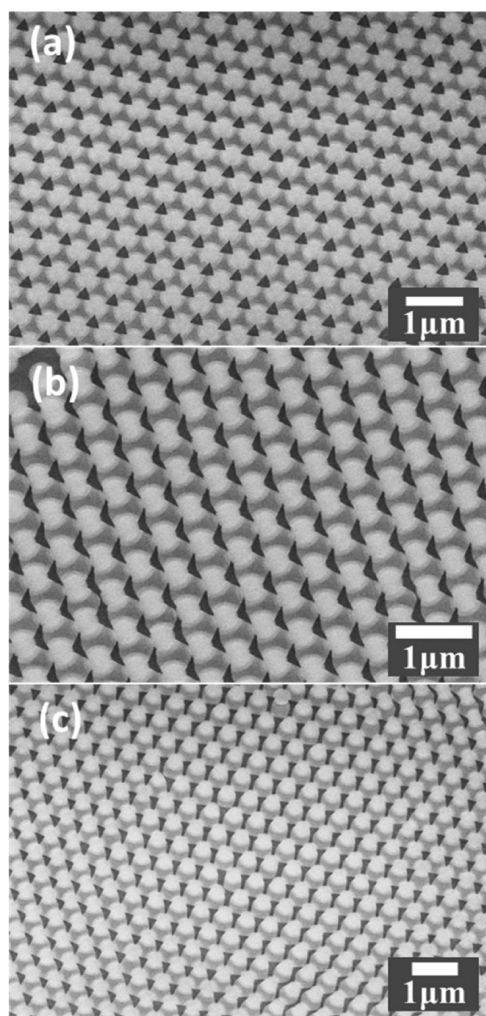


**Figure 5.** SEM images of triangular interstices (a) and their variants (b and c) in the bilayer colloidal crystals after RIE based on M-NSL.

method here. There is no limit on the number of stacked layers, which is a major advantage of this layer-by-layer technique. With the possibility of precisely controlling the angular offsets or the rotational angles between the layers, M-NSL will allow the low-cost fabrication of large-area, quasicrystalline metasurfaces.

**Complementary Gold Nanostructures.** Akin to the widely used NSL in plasmonics, the complex patterns of colloidal crystals created by M-NSL can act as lithographic masks to produce elaborate plasmonic nanostructures on substrates. As a demonstration, we fabricated gold nanostructures of different patterns as shown in the panels a–d in Figure 7. These gold nanostructures closely resemble the patterns of the dark regions (voids) in the SEM images of the colloidal crystals as masks (Figures 3 and 4). As shown in the SEM images, each pattern consists of major micrometer-range Au structures as well as other smaller sub-micrometer Au nanoparticles. Fourier transform infrared (FTIR) transmission measurements (Figure 7e) revealed that each gold pattern exhibits distinctive plasmon resonances,

providing an effective approach toward metasurfaces with tailored optical responses. It is noted that these Au patterns were deposited on a soda glass substrate, which cut off the transmission lower than  $2000\text{ cm}^{-1}$ , resulting in the noise on the spectra. Numerical simulations using the finite-difference time-domain (FDTD) method were carried out to calculate the transmission of the gold patterns in panels a–d. The simulated transmission spectra (Figure 7f) match well with the experimental spectra (Figure 7e), showing the dipole resonances of the elongated structures and the ring-like structures. Although the constituent gold nanoparticles exhibit highly anisotropic shapes, the gold nanopatterns have great polarization stability against the excitation light, as areas of each gold nanopattern contain gold nanoparticles with different orientations. Notably, some of common structures for plasmonics and metamaterials such as bowtie and split-ring antennas are also observed in the SEM images, demonstrating the great potential of M-NSL for fabrication of nanostructures for light manipulation.

## CONCLUSIONS

In conclusion, M-NSL provides an efficient and facile technique for the fabrication of complex patterns and plasmonic nanostructures on substrates. Unlike the conventional NSL, which employs spontaneous self-assembly of colloidal layers, M-NSL exploits the bilayer colloidal crystals made *via* sequential layer stacking that allows the in-plane rotation between the top and bottom layers. The freedom of relative movement between the top and bottom layer leads to the formation of moiré patterns that are thermodynamically unfavorable in the self-assembly process. Combined with dry etching and physical vapor deposition, these moiré patterns gave rise to a variety of novel plasmonic nanostructures. Such metal nanostructures with dimensions ranging from sub-micrometer to several micrometers, together with the abundant sharp features and nanogaps, show potential applications in surface-enhanced optical spectroscopy and biochemical sensing.

It is of great importance to be able to further develop M-NSL and widen its applications. First, we need to obtain large-area single-crystal nanosphere monolayers. Currently we have domain sizes on the order of  $60\text{--}70\ \mu\text{m}^2$ . Larger single crystals will facilitate the construction of robust patterns. Second, techniques for the precise control of relative rotational angles between the neighboring layers are highly desired in order to obtain rationally designed moiré patterns. Lastly, controllable stacking of trilayers or multilayers needs to be realized. Current random stacking results in reduced size of the moiré pattern as more layers are added. These randomly stacked layers present challenges for subsequent etching and material deposition. With the above achievements, M-NSL will

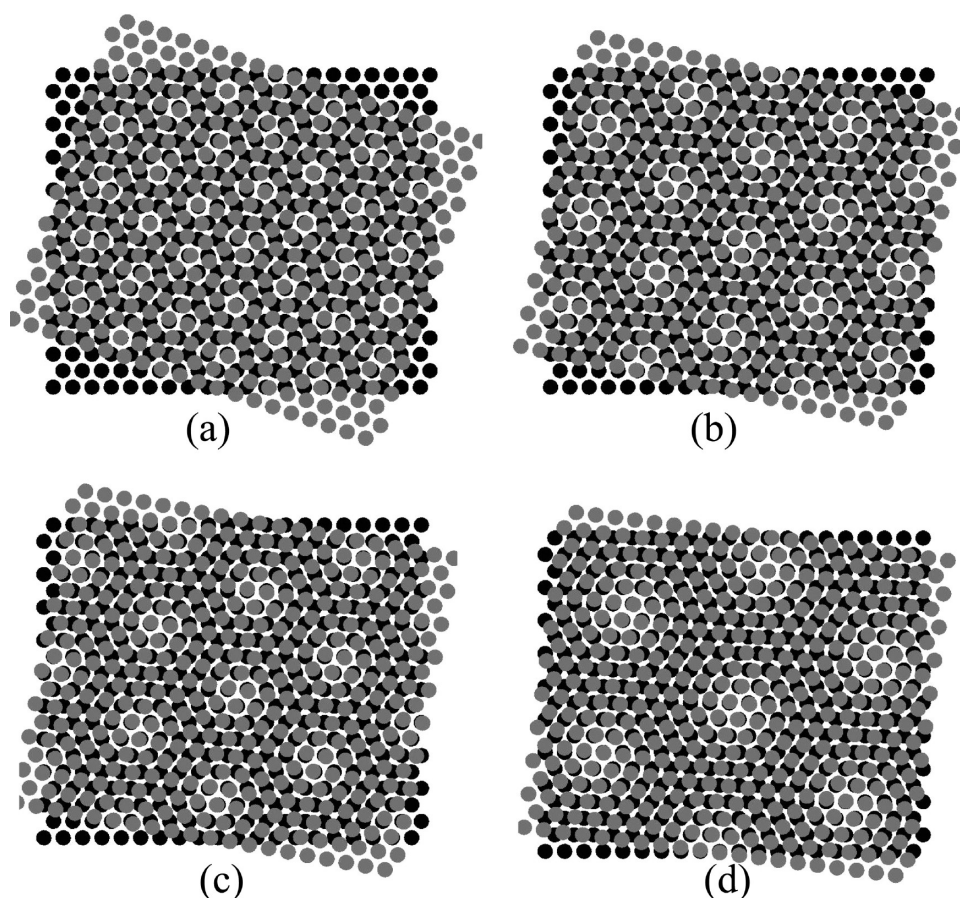


**Figure 6.** Illustration of relative rotation of (a) 19°, (b) 12°, (c) 9°, and (d) 7.5° between the bottom (black) and top (gray) monolayers of spheres, leading to the formation of various moiré patterns.

enable high-throughput, low-cost, robust fabrication of a variety of moiré patterns. The use of different sizes of nanospheres and variable combinations of the

etching and deposition parameters will further enrich achievable patterns and metasurfaces with tailored properties for a wide range of applications.

## METHODS

**Materials.** Sulfate-functionalized polystyrene nanospheres (~4%, Thermo Scientific Inc.) with a diameter of 510 nm were concentrated by centrifugation at 2000g for 10 min. The nanospheres were finally dispersed, ~10%, in a DI water/ethanol mixture (1:1 volume ratio) with ultrasonication. Small glass substrates (1 × 2 cm) were cut from regular soda-lime glass slide (1-9645-01, AS ONE Corporation, Japan) and cleaned by 5 min ultrasonication in acetone, ethanol, and DI water. The substrates were further cleaned in a mixture of NH<sub>4</sub>OH/H<sub>2</sub>O<sub>2</sub>/H<sub>2</sub>O (1:1:5 volume ratio) at 80 °C, leading to hydrophilic surfaces. Finally, the substrates were washed with copious DI water and stored in DI water.

**Fabrication.** A plastic container (polystyrene, 70 × 40 × 15 mm, AS ONE Corporation, Japan) was used as the water reservoir, as shown in Figure 1a. The container was tilted ~5° from the laboratory table surface. The sphere suspensions were dispersed onto the tilted glass slide, as shown in Figure 1a. The sphere suspensions flow toward the water–air–glass intersection before they spread out at the water–air interface. After a monolayer of spheres is formed on the water surface, the water is slowly drained out of the container with a syringe pump (NE-1000X, New Era Pump Systems, Inc.), transferring the monolayer of spheres onto a clean substrate or onto another monolayer of spheres on the substrate. Finally the samples were left to dry in ambient environment.

It is noted that, for the second (or top) layer deposition, extra efforts were taken to submerge the substrates with the first (or bottom) layers in water to avoid the release of the first layers from the substrates by the large surface tension of water. Specifically, the substrates were first left in ethanol solution in the tilted container. We slowly added water into the ethanol and subsequently drained the mixtures. For each cycle of draining, enough solution was left in the container to keep the substrates submerged. We repeated this process until the solution in the container was almost 100% water, upon which the submerged substrates with the monolayers remained intact.

Dry etching of the bilayer colloidal crystals was performed inside a commercial ICP (inductively coupled plasma)-RIE system (CE-300I, ULVAC Inc.) with O<sub>2</sub> plasma (20 sccm, antenna RF power of 200 W, and bias RF power of 5 W). The etching time is ~90 s. Using the etched crystals as masks, we deposited 5 nm of Cr and 70 nm of gold onto the samples by electron-beam deposition (UEP-3000-2C, ULVAC Inc.). The Cr film served as the adhesion layer between gold and glass substrates. The PS crystals were selectively removed by ultrasonication of the samples in toluene for 5 min. SEM images of the colloidal crystals and the gold nanostructures were collected using a Hitachi FE-SEM (SU8200).

**FTIR Measurements.** The optical transmission spectra of gold nanostructures were recorded with an FTIR microscope (Continuum, Thermo Fisher Scientific Inc.) with a 50 × 50 μm<sup>2</sup>

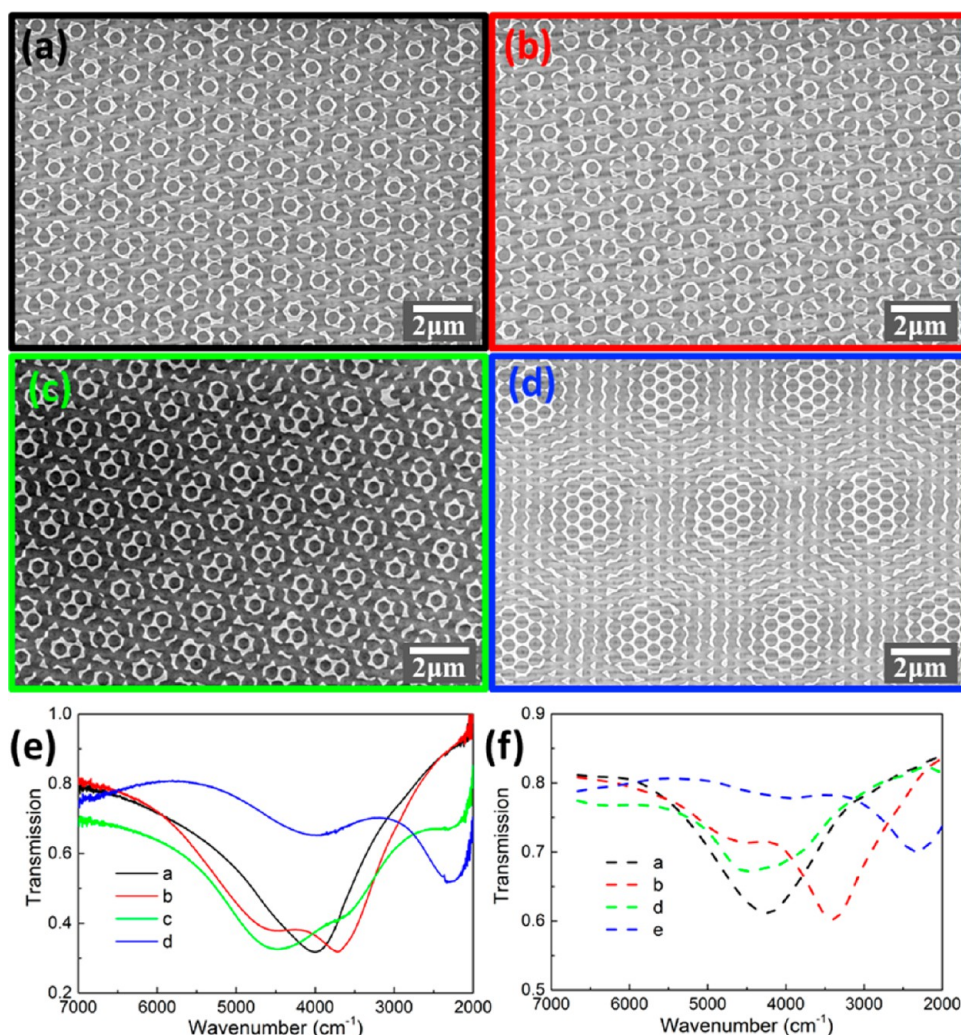


**Figure 7.** SEM images of the complementary gold nanostructures on glass substrates based on M-NSL (a–d) and the corresponding experimental FTIR transmission spectra (e) and the simulated spectra (f).

aperture. During the measurements, the microscope interior was constantly purged with  $N_2$  while the samples were exposed to air on the sample stage. We used a feature known as “automatic atmospheric suppression” in the microscope software OMNIC (version 9, Thermo Fisher Scientific Inc.) to remove the  $CO_2$  and  $H_2O$  absorption lines. This feature does not interfere with the acquisition of the spectra. The transmitted light through the samples was collected using a liquid-nitrogen-cooled mercury cadmium telluride (MCT) detector. The transmittance was calculated using a plain glass slide as the reference.

**FDTD Simulations.** Numerical simulations on the optical properties of gold nanostructures were conducted using the commercially available package FDTD Solutions from Lumerical Inc. The geometries of the gold nanostructures used in the simulations were from the models directly imported from the SEM images. Normally incident plane waves were used as light sources. The transmitted light was collected by a two-dimensional detector that was positioned below the gold nanostructures. Perfectly matched layers (PMLs) were applied at all boundaries. The refractive index of the glass substrate was set to be 1.4, and the optical constants of gold in the infrared region were obtained from ref 52.

**Conflict of Interest:** The authors declare no competing financial interest.

**Acknowledgment.** Y.B.Z. acknowledges the financial support of the Beckman Young Investigator Program. K.C. acknowledges the technical support on dry etching and electron-beam deposition from MANA Foundry.

**Supporting Information Available:** SEM images of etched bilayer crystals formed by conventional spontaneous self-assembly. The Supporting Information is available free of charge on the ACS Publications website at DOI: 10.1021/acsnano.5b00978.

## REFERENCES AND NOTES

- Hulteen, J. C.; Van Duyne, R. P. Nanosphere Lithography: A Materials General Fabrication Process for Periodic Particle Array Surfaces. *J. Vac. Sci. Technol. A* **1995**, *13*, 1553–1558.
- Chen, K.; Durak, C.; Heflin, J. R.; Robinson, H. D. Plasmon-Enhanced Second-Harmonic Generation from Ionic Self-Assembled Multilayer Films. *Nano Lett.* **2007**, *7*, 254–258.
- Haynes, C. L.; Van Duyne, R. P. Nanosphere Lithography: A Versatile Nanofabrication Tool for Studies of Size-Dependent Nanoparticle Optics. *J. Phys. Chem. B* **2001**, *105*, 5599–5611.
- Zheng, Y. B.; Jensen, L.; Yan, W.; Walker, T. R.; Juluri, B. K.; Jensen, L.; Huang, T. J. Chemically Tuning the Localized Surface Plasmon Resonances of Gold Nanostructure Arrays. *J. Phys. Chem. C* **2009**, *113*, 7019–7024.
- Zheng, Y. B.; Juluri, B. K.; Mao, X.; Walker, T. R.; Huang, T. J. Systematic Investigation of Localized Surface Plasmon Resonance of Long-Range Ordered Au Nanodisk Arrays. *J. Appl. Phys.* **2008**, *103*, 014308.
- Vogel, N.; Fischer, J.; Mohammadi, R.; Retsch, M.; Butt, H.-J. r.; Landfester, K.; Weiss, C. K.; Kreiter, M. Plasmon Hybridization in Stacked Double Crescents Arrays

- Fabricated by Colloidal Lithography. *Nano Lett.* **2011**, *11*, 446–454.
7. Lu, Y.; Liu, G. L.; Kim, J.; Mejia, Y. X.; Lee, L. P. Nanophotonic Crescent Moon Structures with Sharp Edge for Ultrasensitive Biomolecular Detection by Local Electromagnetic Field Enhancement Effect. *Nano Lett.* **2004**, *5*, 119–124.
  8. Bukasov, R.; Ali, T. A.; Nordlander, P.; Shumaker-Parry, J. S. Probing the Plasmonic Near-Field of Gold Nanocrescent Antennas. *ACS Nano* **2010**, *4*, 6639–6650.
  9. Kosiorok, A.; Kandulski, W.; Glaczynska, H.; Giersig, M. Fabrication of Nanoscale Rings, Dots, and Rods by Combining Shadow Nanosphere Lithography and Annealed Polystyrene Nanosphere Masks. *Small* **2005**, *1*, 439–444.
  10. Zhao, J.; Frank, B.; Burger, S.; Giessen, H. Large-Area High-Quality Plasmonic Oligomers Fabricated by Angle-Controlled Colloidal Nanolithography. *ACS Nano* **2011**, *5*, 9009–9016.
  11. Kosiorok, A.; Kandulski, W.; Chudzinski, P.; Kempa, K.; Giersig, M. Shadow Nanosphere Lithography: Simulation and Experiment. *Nano Lett.* **2004**, *4*, 1359–1363.
  12. Gwinner, M. C.; Koroknay, E.; Fu, L.; Patoka, P.; Kandulski, W.; Giersig, M.; Giessen, H. Periodic Large-Area Metallic Split-Ring Resonator Metamaterial Fabrication Based on Shadow Nanosphere Lithography. *Small* **2009**, *5*, 400–406.
  13. Zheng, Y.; Wang, S.; Huan, A.; Wang, Y. Fabrication of Large Area Ordered Metal Nanoring Arrays for Nanoscale Optical Sensors. *J. Non-Cryst. Solids* **2006**, *352*, 2532–2535.
  14. Hoffmann, J. M.; Yin, X.; Richter, J.; Hartung, A.; Maß, T. W. W.; Taubner, T. Low-Cost Infrared Resonant Structures for Surface-Enhanced Infrared Absorption Spectroscopy in the Fingerprint Region from 3 to 13  $\mu\text{m}$ . *J. Phys. Chem. C* **2013**, *117*, 11311–11316.
  15. Honda, M.; Kumamoto, Y.; Taguchi, A.; Saito, Y.; Kawata, S. Plasmon-Enhanced UV Photocatalysis. *Appl. Phys. Lett.* **2014**, *104*, 061108–061111.
  16. Hsiao, V. K. S.; Zheng, Y. B.; Juluri, B. K.; Huang, T. J. Light-Driven Plasmonic Switches Based on Au Nanodisk Arrays and Photoresponsive Liquid Crystals. *Adv. Mater.* **2008**, *20*, 3528–3532.
  17. Zheng, Y. B.; Yang, Y.-W.; Jensen, L.; Fang, L.; Juluri, B. K.; Flood, A. H.; Weiss, P. S.; Stoddart, J. F.; Huang, T. J. Active Molecular Plasmonics: Controlling Plasmon Resonances with Molecular Switches. *Nano Lett.* **2009**, *9*, 819–825.
  18. Zheng, Y. B.; Kiraly, B.; Cheunkar, S.; Huang, T. J.; Weiss, P. S. Incident-Angle-Modulated Molecular Plasmonic Switches: A Case of Weak Exciton–Plasmon Coupling. *Nano Lett.* **2011**, *11*, 2061–2065.
  19. Zayats, A. V.; Maier, S. *Active Plasmonics and Tuneable Plasmonic Metamaterials*; John Wiley & Sons, Inc.: New York, 2013; p 336.
  20. Haes, A. J.; Van Duyne, R. P. A Nanoscale Optical Biosensor: Sensitivity and Selectivity of an Approach Based on the Localized Surface Plasmon Resonance Spectroscopy of Triangular Silver Nanoparticles. *J. Am. Chem. Soc.* **2002**, *124*, 10596–10604.
  21. Zhang, G.; Wang, D.; Möhwald, H. Ordered Binary Arrays of Au Nanoparticles Derived from Colloidal Lithography. *Nano Lett.* **2006**, *7*, 127–132.
  22. Nemiroski, A.; Gonidec, M.; Fox, J. M.; Jean-Remy, P.; Turnage, E.; Whitesides, G. M. Engineering Shadows to Fabricate Optical Metasurfaces. *ACS Nano* **2014**, *8*, 11061–11070.
  23. Choi, J.-Y.; Alford, T. L.; Honsberg, C. B. Solvent-Controlled Spin-Coating Method for Large-Scale Area Deposition of Two-Dimensional Silica Nanosphere Assembled Layers. *Langmuir* **2014**, *30*, 5732–5738.
  24. Dimitrov, A. S.; Nagayama, K. Continuous Convective Assembling of Fine Particles into Two-Dimensional Arrays on Solid Surfaces. *Langmuir* **1996**, *12*, 1303–1311.
  25. Prevo, B. G.; Velev, O. D. Controlled, Rapid Deposition of Structured Coatings of Micro- and Nanoparticle Suspensions. *Langmuir* **2004**, *20*, 2099–2107.
  26. Sirotkin, E.; Apweiler, J. D.; Ogrin, F. Y. Macroscopic Ordering of Polystyrene Carboxylate-Modified Nanospheres Self-Assembled at the Water–Air Interface. *Langmuir* **2010**, *26*, 10677–10683.
  27. Park, S. H.; Qin, D.; Xia, Y. Crystallization of Mesoscale Particles over Large Areas. *Adv. Mater.* **1998**, *10*, 1028–1032.
  28. Cong, H.; Cao, W. Colloidal Crystallization Induced by Capillary Force. *Langmuir* **2003**, *19*, 8177–8181.
  29. Chen, K.; Stoianov, S. V.; Bangerter, J.; Robinson, H. D. Restricted Meniscus Convective Self-Assembly. *J. Colloid Interface Sci.* **2010**, *344*, 315–320.
  30. Choi, D.-G.; Yu, H. K.; Jang, S. G.; Yang, S.-M. Colloidal Lithographic Nanopatterning via Reactive Ion Etching. *J. Am. Chem. Soc.* **2004**, *126*, 7019–7025.
  31. Yang, S.-M.; Jang, S. G.; Choi, D.-G.; Kim, S.; Yu, H. K. Nanomachining by Colloidal Lithography. *Small* **2006**, *2*, 458–475.
  32. Bassett, G. A.; Menter, J. W.; Pashley, D. W. Moiré Patterns on Electron Micrographs, and Their Application to the Study of Dislocations in Metals. *Proc. R. Soc. A* **1958**, *246*, 345–368.
  33. Liu, S.; Zhang, X.; Lai, H. Artistic Effect and Application of Moiré Patterns in Security Holograms. *Appl. Opt.* **1995**, *34*, 4700–4702.
  34. Van Renesse, R. L. *Optical Document Security*; Artech House: London, 2004; p 386.
  35. Amidror, I.; Chosson, S.; Hersch, R. D. Moiré Methods for the Protection of Documents and Products: A Short Survey. *J. Phys.: Conf. Ser.* **2007**, *77*, 012001.
  36. Nishijima, Y.; Oster, G. Moiré Patterns: Their Application to Refractive Index and Refractive Index Gradient Measurements. *J. Opt. Soc. Am.* **1964**, *54*, 1–4.
  37. Lubin, S. M.; Zhou, W.; Hryn, A. J.; Huntington, M. D.; Odom, T. W. High-Rotational Symmetry Lattices Fabricated by Moiré Nanolithography. *Nano Lett.* **2012**, *12*, 4948–4952.
  38. Lubin, S. M.; Hryn, A. J.; Huntington, M. D.; Engel, C. J.; Odom, T. W. Quasiperiodic Moiré Plasmonic Crystals. *ACS Nano* **2013**, *7*, 11035–11042.
  39. Gao, H.; Zhou, W.; Odom, T. W. Plasmonic Crystals: A Platform to Catalog Resonances from Ultraviolet to Near-Infrared Wavelengths in a Plasmonic Library. *Adv. Funct. Mater.* **2010**, *20*, 529–539.
  40. Kasture, S.; Ravishankar, A. P.; Yallapragada, V. J.; Patil, R.; Valappil, N. V.; Mulay, G.; Achanta, V. G. Plasmonic Quasiperiodic Crystals with Broadband Transmission Enhancement. *Sci. Rep.* **2014**, *4*, 5257.
  41. Bauer, C.; Kobiela, G.; Giessen, H. 2D Quasiperiodic Plasmonic Crystals. *Sci. Rep.* **2012**, *2*, 681.
  42. Biagioni, P.; Huang, J.-S.; Hecht, B. Nanoantennas for Visible and Infrared Radiation. *Rep. Prog. Phys.* **2012**, *75*, 024402.
  43. Novotny, L.; van Hulst, N. Antennas for Light. *Nat. Photonics* **2011**, *5*, 83–90.
  44. Kildishev, A. V.; Boltasseva, A.; Shalaev, V. M. Planar Photonics with Metasurfaces. *Science* **2013**, *339*, 1232009.
  45. Yu, N.; Capasso, F. Flat Optics with Designer Metasurfaces. *Nat. Mater.* **2014**, *13*, 139–150.
  46. Lin, D.; Fan, P.; Hasman, E.; Brongersma, M. L. Dielectric Gradient Metasurface Optical Elements. *Science* **2014**, *345*, 298–302.
  47. Xu, P.; Qi, D.; Schoelz, J. K.; Thompson, J.; Thibado, P. M.; Wheeler, V. D.; Nyakiti, L. O.; Myers-Ward, R. L.; Eddy, C. R., Jr.; Gaskill, D. K.; Neek-Amal, M.; Peeters, F. M. Multilayer Graphene, Moiré Patterns, Grain Boundaries and Defects Identified by Scanning Tunneling Microscopy on the M-Plane, Non-polar Surface of SiC. *Carbon* **2014**, *80*, 75–81.
  48. Cho, S.-Y.; Jeon, H.-J.; Kim, J.-S.; Ok, J. M.; Jung, H.-T. Hierarchical Ordering of Quantum Dots and Liquid with Tunable Super-Periodicity into High Aspect Ratio Moiré Superlattice Structure. *Adv. Funct. Mater.* **2014**, *24*, 6939–6947.
  49. Luchnikov, V.; Kondyurin, A.; Formanek, P.; Lichte, H.; Stamm, M. Moiré Patterns in Superimposed Nanoporous Thin Films Derived from Block-Copolymer Assemblies. *Nano Lett.* **2007**, *7*, 3628–3632.
  50. Koller, D. M.; Hohenester, U.; Hohenau, A.; Ditlbacher, H.; Reil, F.; Galler, N.; Aussenegg, F. R.; Leitner, A.; Trügler, A.

- Krenn, J. R. Superresolution Moiré Mapping of Particle Plasmon Modes. *Phys. Rev. Lett.* **2010**, *104*, 143901.
51. Balci, S.; Karabiyik, M.; Kocabas, A.; Kocabas, C.; Aydinli, A. Coupled Plasmonic Cavities on Moire Surfaces. *Plasmonics* **2010**, *5*, 429–436.
52. Palik, E. D. *Handbook of Optical Constants of Solids*. Elsevier: Amsterdam, 1998.